

Accelerated Article Preview**Loss of furin cleavage site attenuates SARS-CoV-2 pathogenesis**

Received: 26 August 2020

Accepted: 13 January 2021

Accelerated Article Preview Published online 25 January 2021

Cite this article as: Johnson, B. A. et al. Loss of furin cleavage site attenuates SARS-CoV-2 pathogenesis. *Nature* <https://doi.org/10.1038/s41586-021-03237-4> (2021).

Bryan A. Johnson, Xuping Xie, Adam L. Bailey, Birte Kalveram, Kumari G. Lokugamage, Antonio Muruato, Jing Zou, Xianwen Zhang, Terry Juelich, Jennifer K. Smith, Lihong Zhang, Nathen Bopp, Craig Schindewolf, Michelle Vu, Abigail Vanderheiden, Emma S. Winkler, Daniele Swetnam, Jessica A. Plante, Patricia Aguilar, Kenneth S. Plante, Vsevolod Popov, Benhur Lee, Scott C. Weaver, Mehul S. Suthar, Andrew L. Routh, Ping Ren, Zhiqiang Ku, Zhiqiang An, Kari Debbink, Michael S. Diamond, Pei Yong Shi, Alexander N. Freiberg & Vineet D. Menachery

This is a PDF file of a peer-reviewed paper that has been accepted for publication. Although unedited, the content has been subjected to preliminary formatting. Nature is providing this early version of the typeset paper as a service to our authors and readers. The text and figures will undergo copyediting and a proof review before the paper is published in its final form. Please note that during the production process errors may be discovered which could affect the content, and all legal disclaimers apply.

Loss of furin cleavage site attenuates SARS-CoV-2 pathogenesis

<https://doi.org/10.1038/s41586-021-03237-4>

Received: 26 August 2020

Accepted: 13 January 2021

Published online: 25 January 2021

Bryan A. Johnson^{1,14}, Xuping Xie^{2,14}, Adam L. Bailey^{5,14}, Birte Kalveram³, Kumari G. Lokugamage¹, Antonio Muruato¹, Jing Zou², Xianwen Zhang², Terry Juelich³, Jennifer K. Smith³, Lihong Zhang³, Nathen Bopp³, Craig Schindewolf¹, Michelle Vu¹, Abigail Vanderheiden^{5,6,7}, Emma S. Winkler^{5,12}, Daniele Swetnam², Jessica A. Plante¹, Patricia Aguilar³, Kenneth S. Plante¹, Vsevolod Popov³, Benhur Lee⁹, Scott C. Weaver^{1,4}, Mehul S. Suthar^{6,7,8}, Andrew L. Routh², Ping Ren³, Zhiqiang Ku¹⁰, Zhiqiang An¹⁰, Kari Debbink¹¹, Michael S. Diamond^{5,12,13}, Pei Yong Shi^{2,4,15}, Alexander N. Freiberg^{3,4,15} & Vineet D. Menachery^{1,4,15}✉

SARS-CoV-2, a novel coronavirus (CoV)-producing worldwide pandemic¹, has a furin cleavage site (PRRAR) in its spike protein that is absent in other group 2B CoVs². To explore whether the furin cleavage site contributes to infection and pathogenesis, we generated a mutant SARS-CoV-2 deleting the furin cleavage site (Δ PRRA). SARS-CoV-2 Δ PRRA replicates had faster kinetics, improved fitness in Vero E6 cells, and reduced spike protein processing as compared to parental SARS-CoV-2. However, the Δ PRRA mutant had reduced replication in a human respiratory cell line and was attenuated in both hamster and K18-hACE2 transgenic mouse models of SARS-CoV-2 pathogenesis. Despite reduced disease, the Δ PRRA mutant conferred protection against rechallenge with the parental SARS-CoV-2. Importantly, COVID-19 patient sera and receptor-binding domain (RBD) monoclonal antibodies had lower neutralization values against the Δ PRRA mutant versus parental SARS-CoV-2, likely due to increased particle/PFU ratio. Together, these results demonstrate a critical role for the furin cleavage site in SARS-CoV-2 infection and highlight the importance of this site in evaluating antibody neutralization activity.

The emergence of severe acute respiratory syndrome coronavirus 2 (SARS-CoV-2) has ushered in a worldwide pandemic^{1,3}. The novel coronavirus, like severe acute respiratory syndrome (SARS)-CoV and Middle East Respiratory Syndrome (MERS)-CoV, induces severe respiratory disease including fever, multi-lobe pneumonia, and in many cases, death⁴. While SARS-CoV-2 shares a similar genomic structure and protein homology with SARS-CoV, its ability to spread asymptotically and cause mild to severe disease distinguishes it from the earlier pandemic CoV⁵. Examining the spike (S) protein, a glycoprotein responsible for receptor binding and entry following cleavage at its S1/S2 and S2 sites (Extended Data Fig. 1a), studies indicate that SARS-CoV-2 has greater affinity for the ACE2 receptor than SARS-CoV⁶. Notably, attention has focused on a furin cleavage motif at the S1/S2 cleavage site². Absent in other group 2B CoVs, the four amino acids (PRRA) form a RXXR cleavage motif for serine proteases when added to S1/S2 cleavage site (PRRAR, Extended Data Fig. 1b)⁷. Structural analysis has shown that furin cleavage facilitates a higher proportion of spike to bind human ACE2 receptor⁸ and may have facilitated the

emergence of SARS-CoV-2 in humans. To date, the furin cleavage site has been analyzed using mutated pseudotyped viruses that ablate the spike's ability to mediate cell-cell and virus-cell fusion in Calu-3 cells^{9,10}. Other studies have isolated deletion variants of SARS-CoV-2 that span the furin cleavage and S1/S2 site attenuating infection^{11,12}. To date, no studies have evaluated the function of the furin site using authentic SARS-CoV-2 containing a precise PRRA deletion. Such studies are necessary as discrepant results reported for the spike D614G mutation highlight differences between pseudotyped and authentic SARS-CoV-2 variants^{13,14}.

Here, we utilized a reverse genetic system to generate a SARS-CoV-2 mutant lacking the spike furin cleavage site (Δ PRRA)¹⁵. The PRRA deletion reduced spike protein cleavage, but augmented viral replication in Vero E6 cells. Ectopic expression of TMPRSS2 in Vero E6 cells removed the fitness advantage for Δ PRRA. In contrast, the Δ PRRA mutant was attenuated in a human respiratory cell line and had reduced viral pathogenesis in both hamsters and K18-hACE2 expressing mice. Notably, the Δ PRRA mutation required more antisera and monoclonal

¹Department of Microbiology and Immunology, University of Texas Medical Branch, Galveston, TX, USA. ²Department of Biochemistry and Molecular Biology, University of Texas Medical Branch, Galveston, TX, USA. ³Department of Pathology, University of Texas Medical Branch, Galveston, TX, USA. ⁴Institute for Human Infection and Immunity, University of Texas Medical Branch, Galveston, TX, USA. ⁵Department of Pathology & Immunology, Washington University School of Medicine, St. Louis, MO, USA. ⁶Department of Pediatrics, Emory University School of Medicine, Atlanta, GA, USA. ⁷Emory Vaccine Center, Emory University School of Medicine, Atlanta, GA, USA. ⁸Yerkes National Primate Research Center, Atlanta, GA, USA. ⁹Icahn School of Medicine at Mount Sinai, New York, NY, USA. ¹⁰Texas Therapeutics Institute, Brown Foundation Institute of Molecular Medicine, University of Texas Health Science Center at Houston, Houston, USA. ¹¹Bowie State University, Bowie, MD, USA. ¹²Department of Medicine, Washington University School of Medicine, St. Louis, MO, USA. ¹³Department of Molecular Microbiology, Washington University School of Medicine, St. Louis, MO, USA. ¹⁴These authors contributed equally: Bryan A. Johnson, Xuping Xie, Adam L. Bailey. ¹⁵These authors jointly supervised this work: Pei Yong Shi, Alexander N. Freiberg, Vineet D. Menachery. ✉e-mail: vimenach@utmb.edu

antibodies targeting the receptor-binding domain (RBD) for neutralization. Our results demonstrate a critical role of the furin cleavage site in SARS-CoV-2 infection and highlight the concerns when using the furin deletion variants for COVID-19 research.

Generation of the Δ PRRA mutant

We generated a mutant virus lacking the PRRA motif using a SARS-CoV-2 reverse genetic system (Fig. 1a)¹⁵. The furin cleavage site resides in an exterior and ostensibly unresolved loop of the SARS-CoV-2 spike structure below the globular head and away from the RBD (Fig. 1b). We used homology modeling to visualize the PRRA site in this extended loop (cyan). Deletion of the PRRA motif is predicted to shorten the loop without disrupting the overall structure of the spike. Following electroporation, we recovered Δ PRRA mutant SARS-CoV-2 with a titer equivalent to the wild-type (WT) virus. Unexpectedly, the Δ PRRA virus produced a larger plaque size on Vero E6 cells than WT virus, suggesting changes in viral replication and spread in the absence of the furin cleavage site (Extended Data Fig. 1c).

Distinct Δ PRRA replication and cleavage

To evaluate viral replication, we inoculated Vero E6 cells with WT and Δ PRRA SARS-CoV-2. SARS-CoV-2 replicates robustly in Vero E6 cells, which often are used for virus stock propagation and inactivated vaccine production¹⁶. Following a low multiplicity of infection (MOI of 0.01 plaque forming units (PFU)/cell), both WT and Δ PRRA viruses replicated to similar end-point titers. However, Δ PRRA mutant had a 25-fold higher viral titer and more cytopathic effect (CPE) at 24 hours post infection (HPI) (Fig. 1c). Thus, the loss of the furin cleavage site augments SARS-CoV-2 replication in Vero E6 cells.

We next evaluated spike processing of the Δ PRRA mutant relative to WT SARS-CoV-2 and SARS-CoV. Vero E6 cells were inoculated at an MOI of ~0.1 for 24 h, and virions purified virions were isolated using sucrose cushion ultracentrifugation. The pelleted virus was examined for spike processing and nucleocapsid (N) protein by western blotting. Following SARS-CoV infection, the majority of the spike protein is in its full-length form (98.6%) (Fig. 1d, Extended Data Fig. 2a, uncropped images in Supplementary Fig. 1 & 2), consistent with minimal processing. In contrast, the WT SARS-CoV-2 virions had significant spike protein cleavage, with 59.6% cleaved to S1/S2 products. The Δ PRRA mutant reduced the S1/S2 cleavage amount to 14.5%. Given the similar levels of N protein, these results illustrate the differences between SARS-CoV and SARS-CoV-2, and show that SARS-CoV-2 processing of the spike is driven by the furin cleavage site.

Given the replication advantage at 24 HPI (Fig. 1d), we evaluated the fitness of the Δ PRRA mutant relative to WT SARS-CoV-2 in a competition assay. Using PFU to determine the input, we mixed the WT and mutant at different ratios in Vero E6 cells, and used RT-qPCR to quantify relative fitness 24 HPI (Fig. 1e, Extended Data Fig. 2b-c). At a 50:50 ratio, the Δ PRRA mutant outcompeted WT virus becoming nearly 90% of the viral population at 24h. A 90:10 WT-to-mutant input ratio resulted in the Δ PRRA mutant comprising ~65% of the viral sequences at 24h. The inverse 10:90 WT-to-mutant input ratio produced 97% Δ PRRA, further confirming the advantage mutant in Vero E6 cells. The RT-qPCR results were corroborated with deep sequencing analysis (Extended Data Fig. 2d). Thus, deletion of the furin cleavage site provides a fitness advantage in Vero E6 cells, and may contribute to mutations found in WT SARS-CoV-2 cultured on Vero E6 cells.

Attenuation of Δ PRRA in Calu3 cells

We next evaluated the Δ PRRA mutant in Calu3 2B4 cells, a human lung adenocarcinoma cell line commonly used to study influenza virus and other CoVs¹⁷. In contrast to Vero E6 cells, the Δ PRRA virus replicated less

efficiently than WT (Fig. 1f). At both 48 and 72 HPI, the Δ PRRA mutant had ~10-fold reductions in viral titer indicating the loss of the furin cleavage site impairs viral replication in Calu3. Next, we evaluated spike processing on virions that were produced from Calu3 2B4 cells. Consistent with Vero E6 cells, spike from SARS-CoV was not cleaved to S1/S2. However, ~87.3% of spike from WT SARS-CoV-2 was processed to S1/S2, greater than the 59.6% observed in Vero E6 cells (Fig. 1g, Extended Data Fig. 2e, uncropped images in Supplementary Fig. 1 & 2). Unexpectedly, the Δ PRRA mutant also showed an increase in the S1/S2 cleavage product. This band represented more than twice as much S1/S2 cleavage product (33.1% vs 14.5%) as seen in Vero E6 cell supernatants, although the deletion does result in a major shift from cleaved to uncleaved S protein. While more full-length spike is observed in the WT virus infection, the Calu3 results indicate that even without the furin cleavage site, there is significant processing of the SARS-CoV-2 spike. Thus, factors outside the PRRA motif contribute to cleavage of the SARS-CoV-2 spike in a cell type-dependent manner.

TMPRSS2 reduces Δ PRRA fitness advantage

One distinction between Vero E6 and Calu3 cells is the expression of host serine proteases like TMPRSS2¹⁸. To determine whether this cell surface protease modulates replication of Δ PRRA, we evaluated infection in Vero cells ectopically expressing TMPRSS2. Following low MOI (0.01) infection, both WT and Δ PRRA SARS-CoV-2 replicated to similar levels (Fig. 1h). Next, we performed competition assay to evaluate the fitness of Δ PRRA mutant in the TMPRSS2-Vero E6 cells. With a 50:50 input ratio, the Δ PRRA mutant and WT virus retained equal levels in the TMPRSS2-Vero E6 cells (Fig. 1i). These results demonstrate that expression of TMPRSS2 reduced the Vero E6 replication/fitness advantage of the Δ PRRA mutant over WT SARS-CoV-2. To examine whether TMPRSS2 affects spike cleavage, we purified virions from TMPRSS2-Vero E6 cells and quantified the full-length to S1/S2 spike ratios (Fig. 1j, uncropped images in Supplementary Fig. 3 & 4). Compared with Vero E6 result, the expression of TMPRSS2 had minimal effect on spike processing ratios (compare Extended Data Fig. 2a, f). Both SARS-CoV and Δ PRRA had mostly full-length form of spike intact (96.4% and 95.9%), whereas WT SARS-CoV-2 had nearly half of the spike processed to S1/S2 form (Extended Data Fig. 2f). Overall, the results argue that (i) TMPRSS2 affects virus entry rather than virion release and (ii) TMPRSS2-Vero cells reduces selection of Δ PRRA mutants.

In vivo attenuation of Δ PRRA mutant

We next evaluated Δ PRRA mutant *in vivo* using the hamster model of SARS-CoV-2 pathogenesis¹⁹ using four male hamsters challenged via intranasal (i.n.) inoculation with 10⁵ PFU of WT SARS-CoV-2 or Δ PRRA mutant (Fig. 2a). Following infection with WT SARS-CoV-2, hamsters steadily lost weight starting at day 2 and continuing through day 8 with peak weight loss nearing 15% (Fig. 2b, Extended Data Fig. 3a). Disease scores peaked at day 8, when animals had ruffled fur, hunched posture, and reduced activity requiring additional monitoring (Fig. 2c, Extended Data Fig. 3b). Despite severe disease, the WT-infected hamsters recovered and regained their starting weight by day 15 (Extended Data Fig. 3a). In contrast, hamsters infected with SARS-CoV-2 Δ PRRA showed minimal weight loss and no disease (Fig. 2b, Extended Data Fig. 3a-b). Hamsters in both infection groups gained weight after day 10, over the remainder of the 28-day time course (Extended Data Fig. 3a). In nasal washes, both WT and Δ PRRA infected hamsters had similar viral titers at 2 DPI (Fig. 2d). However, greater Δ PRRA replication was observed at 3 and 4 DPI relative to the WT SARS-CoV-2. In addition, the WT virus was cleared from the nasal washes a day earlier than the Δ PRRA mutant, although no infectious virus was detected after day 7 in either of the hamster groups. For viral RNA from oral swabs, we observed a similar pattern with higher viral RNA concentrations at 3 and 4 DPI in the Δ PRRA mutant relative to WT (Fig. 2e). However, the viral RNA in the swabs stayed positive though 7 DPI with higher concentrations from

the WT than Δ PRRA infected animals. Together, these results suggest that despite attenuated disease, the Δ PRRA mutant replicates efficiently in the oral and nasal cavity of hamsters

Infection with Δ PRRA mutant protects from SARS-CoV-2 rechallenge

With vaccine strategies that mutate the furin cleavage site^{20,21}, we evaluated if infection with Δ PRRA protects from SARS-CoV-2 rechallenge. Hamsters previously infected with WT or the Δ PRRA mutant were rechallenged with 10^3 PFU of WT SARS-CoV-2 at 28 days post primary. Both WT and Δ PRRA infected hamsters were protected from weight loss following rechallenge (Fig. 2f and Extended Data Fig. 3b). However, mild disease (ruffled fur) was observed in one animal previously infected with WT SARS-CoV-2 (Extended Data Fig. 3c). In contrast, Δ PRRA mutant-infected hamsters produced neither weight loss nor disease. Nasal wash titers and viral RNA from oral swabs were significantly reduced compared to initial infection in both groups and infectious virus cleared by 4 DPI (Fig. 2g-h). Primary infection with both Δ PRRA and WT SARS-CoV-2 produced neutralizing antibodies in serum (-1/600 each at day 28) (Fig. 2i) and subsequent rechallenge boosted this activity, though we noted a 2-fold differences in final PRNT50 values with WT versus the Δ PRRA (-1/2000 vs -1/1000). Together, the results indicate the attenuated Δ PRRA infection induces sufficient immunity to protect hamsters from SARS-CoV-2 rechallenge.

Δ PRRA causes attenuated lung disease in K18-hACE2 transgenic mice

To further evaluate pathogenesis, we infected transgenic C57BL/6 mice expressing hACE2 and are permissive for SARS-CoV-2 infection²². Male and female K18-hACE2 mice were inoculated via *i.n.* route with 10^3 PFU of WT or Δ PRRA SARS-CoV-2 (Fig. 3a). K18-hACE2 mice infected with WT SARS-CoV-2 lost significantly more weight than Δ PRRA infected mice starting at 4 DPI and continuing through the end of the experiment (Fig. 3b). Attenuated disease corresponded to reduced viral replication at day 2 in the lung, nasal turbinates, and nasal washes (Fig. 3c-e). Significant differences in viral burden, however, were not observed in lungs or brain at 7 DPI (Fig. 3f). To examine changes to the functional properties of the lung, we mechanically ventilated mice via tracheostomy and measured several respiratory biophysical parameters. K18-hACE2 mice infected with WT SARS-CoV-2 had reduced inspiratory capacity (Fig. 3g), a downward deflection in pressure/volume loop (Fig. 3h), and increased tissue dampening, respiratory resistance, and tissue elastance consistent with restrictive lung disease localized to the alveoli and tissue parenchyma (Extended Data Fig. 4a-d). In contrast, only mild changes in pulmonary mechanics were observed in Δ PRRA mutant infected mice. Histopathology of lungs at 7 DPI revealed greater immune cell infiltrates and more extensive tissue damage in mice infected with WT virus (Fig. 3i-j, Extended Data Fig. 4e) than Δ PRRA virus (Fig. 3k). Finally, inflammatory mediators 7 DPI revealed greater induction of a subset of cytokines and chemokines following WT compared to Δ PRRA infection (Fig. 3l, Extended Data Fig. 4f). Chemokines associated with macrophage/monocyte activation including MCP-1, MIP-1 β , IP-10, and MIG were greater in WT than Δ PRRA infected mice (Fig. 3l). Several other cytokines and chemokines were increased relative to mock infected animals for both WT and Δ PRRA, but trended higher in WT-infected animals (Extended Data Fig. 4f). Together, the data indicates that the Δ PRRA mutant produces reduced disease and replication at early times following SARS-CoV-2 infection.

Assessing antibody neutralization titers for Δ PRRA

We next evaluated furin cleavage site deletion on virus neutralization. To quantitate neutralization, we generated a Δ PRRA mutant containing

a mNeonGreen (mNG) reporter in open reading frame (ORF)7 and compared results to the WT SARS-CoV-2²³ (Fig. 4a). Examining seventeen COVID-19 human sera, we found nearly uniform reduction in PRNT₅₀ values against the Δ PRRA mutant versus WT (Fig. 4b). The lower PRNT₅₀ values were observed in COVID19 serum samples with low, intermediate, or high neutralizing activity (Fig. 4c-e) and averaged a 2.3-fold reduction across the 17 human sera tested. The differences between WT and Δ PRRA were significant for the high and intermediate responders, but below threshold for the low responders due to incomplete neutralization (Extended Data Table S1). The consistency in the reduction may be due to: (a) The spike proteins has an altered conformation in the Δ PRRA virions, restricting access to more cryptic sites on the spike and allowing WT virus to be more readily neutralized by non-RBD antibodies; (b) more intact spike molecules on the virion surface of Δ PRRA virions, requiring more antibodies to neutralize mutant than WT 2. To explore these possibilities, we evaluated neutralization of the Δ PRRA mutant by three mAbs targeting the SARS-CoV-2 RBD (Fig. 4f-h). Each mAb targets a different site in the RBD, but showed similar reductions in neutralization between WT and Δ PRRA. Whereas the results with mAb1 and mAb3 reached significance, low neutralization levels precluded such conclusions with mAb2 (Extended Data Table S1). Altogether, these results highlight differences in antibody neutralization profiles between the WT and Δ PRRA SARS-CoV-2 mutants.

Differences in the PRNT50 values suggest potential physical variation between WT and Δ PRRA virions. One possible explanation is that the Δ PRRA mutant has more full-length spike protein than WT SARS-CoV-2 (Fig. 1d, Extended Data Fig. 2a), which require more antibody for neutralization. To explore this idea, we examined the WT and Δ PRRA mutant virion by transmission electron microscopy (TEM). We evaluated 40 TEM fields of virions from WT and Δ PRRA stocks for morphology and to determine the particle to PFU ratio. Consistent with previous reports, WT SARS-CoV-2 had classic morphology, forming single virions, and had a particle/PFU ratio approaching 20 (Extended Data Fig. 5, Fig. 4i). In contrast, the Δ PRRA mutant stocks showed a particle/PFU ratio approaching 80, and nearly 33% of the particles clustered in group >3 virions (Fig. 4j). The results suggest that the Δ PRRA mutant form clusters of viruses reminiscent of norovirus and HCV cloaked virions^{24,25}, though the mechanism for SARS-CoV-2 clumping remains unclear. Controlling for clumps as single PFU, the particle/PFU ratio drops to approximately 60:1 and is more consistent with the 2- to 3-fold increase in serum required for neutralization. Combined with the increased expression of full-length spike, the clumping results and particle/PFU ratio provide multiple explanations for why the antibody concentrations required for neutralization are higher.

Overall, the loss of the furin cleavage site in the SARS-CoV-2 spike has a major impact on infection and pathogenesis with reduced replication in Calu3 respiratory cells and ablated disease in two SARS-CoV-2 pathogenesis models. These results are consistent with other studies examining in the furin cleavage site^{11,12}. However, despite the attenuated disease, the Δ PRRA mutant has some replication advantages over WT SARS-CoV-2, which may lead to cell culture adaptations, possibly complicating results. The Δ PRRA mutant fitness advantage in Vero E6 cell is consistent with reports of furin cleavage site deletions in SARS-CoV-2 preparations and patient samples^{11,12}. This issue also has implications for manufacturing inactivated COVID19 vaccine on Vero cells²⁶. Similarly, the shift in antibody neutralization of the Δ PRRA virus indicates the possibility of imprecise results²⁷. With potential vaccine and therapeutics decisions resting on neutralization values, accuracy is an important issue.

A number of approaches can prevent the emergence of the Δ PRRA mutation in SARS-CoV-2 stocks. In our studies, we found no evidence for Δ PRRA deletion in infectious clone derived WT SARS-CoV-2 through passage 2. By utilizing low passage stocks, the incorporation of this

mutation was limited. One alternative uses Vero E6 cell expressing TMPRSS2 to remove the fitness advantage of the Δ PRRA mutant allowing virus propagation without altering the full-length to S1/S2 processing ratio of its spike protein. However, continued passage risks this or other tissue culture adaptations, and careful monitoring of stock composition is needed. Using plaque purification techniques, WT SARS-CoV-2 can be selected for by its smaller plaque morphology.

The furin cleavage site promotes increased spike cleavage in SARS-CoV-2 that has implications for pathogenesis. As such, vaccines and therapeutics that target the furin cleavage site offer an attractive approach to disrupt COVID-19 infection²⁰ and could have implications for other CoVs with furin cleavages sites including HKU1-CoV, OC43-CoV, and MERS-CoV. Disruption or improvement of these furin sites could change the trajectory of disease caused by these CoV. In our studies, the Δ PRRA mutant attenuates disease *in vivo* and confers protection from subsequent rechallenge. However, Δ PRRA replication was not ablated, and substantial tissue damage was observed in both *in vivo* pathogenesis models. Importantly, differences in the PRNT50 values suggest potential antigenic differences between WT and the Δ PRRA mutant that could impact vaccination approaches. Strategies that disrupt or ablate the furin cleavage site might result in altered adaptive immune responses if the mutations occurred in dominant epitopes. For example, based on structural studies, loss of the furin site could reduce access to the more open form of the spike necessary to interact with hACE2 receptor and alter the targets for antibody generation⁸. While the attenuation of the Δ PRRA mutant holds promise vaccine development, further studies are needed to fully explore the extent of antibody and cell-based immunity induced by this mutant.

Overall, our data illustrate the critical role that the furin cleavage site has in SARS-CoV-2 infection and pathogenesis. In its absence, the mutant Δ PRRA virus is attenuated in its ability to replicate in certain cell types and cause disease *in vivo*. However, the results are complicated by augmented replication and fitness in Vero E6 cells driven by the absence of TMPRSS2 expression. Similarly, altered antibody neutralization profiles indicate a critical need to survey this mutation in analysis of SARS-CoV-2 treatments and vaccines. Overall, the work highlights the critical nature of the furin cleavage site in understanding spike protein biology and SARS-CoV-2 infection and pathogenesis.

Online content

Any methods, additional references, Nature Research reporting summaries, source data, extended data, supplementary information, acknowledgements, peer review information; details of author contributions and competing interests; and statements of data and code availability are available at <https://doi.org/10.1038/s41586-021-03237-4>.

1. Gralinski, L.E. & Menachery, V.D. Return of the Coronavirus: 2019-nCoV. *Viruses* **12**(2020).
2. Coutard, B., et al. The spike glycoprotein of the new coronavirus 2019-nCoV contains a furin-like cleavage site absent in CoV of the same clade. *Antiviral Res* **176**, 104742 (2020).
3. Dong, E., Du, H. & Gardner, L. An interactive web-based dashboard to track COVID-19 in real time. *Lancet Infect Dis* **20**, 533-534 (2020).
4. Huang, C., et al. Clinical features of patients infected with 2019 novel coronavirus in Wuhan, China. *Lancet* **395**, 497-506 (2020).
5. Gao, Z., et al. A Systematic Review of Asymptomatic Infections with COVID-19. *J Microbiol Immunol Infect* (2020).
6. Shang, J., et al. Structural basis of receptor recognition by SARS-CoV-2. *Nature* **581**, 221-224 (2020).
7. Seidah, N.G. & Chretien, M. Proprotein and prohormone convertases: a family of subtilases generating diverse bioactive polypeptides. *Brain Res* **848**, 45-62 (1999).
8. Wrobel, A.G., et al. SARS-CoV-2 and bat RaTG13 spike glycoprotein structures inform on virus evolution and furin-cleavage effects. *Nature structural & molecular biology* **27**, 763-767 (2020).
9. Hoffmann, M., Kleine-Weber, H. & Pöhlmann, S. A Multibasic Cleavage Site in the Spike Protein of SARS-CoV-2 Is Essential for Infection of Human Lung Cells. *Mol Cell* **78**, 779-784.e775 (2020).
10. Bestle, D., et al. TMPRSS2 and furin are both essential for proteolytic activation of SARS-CoV-2 in human airway cells. *Life science alliance* **3** (2020).
11. Lau, S.Y., et al. Attenuated SARS-CoV-2 variants with deletions at the S1/S2 junction. *Emerging microbes & infections* **9**, 837-842 (2020).
12. Klimstra, W.B., et al. SARS-CoV-2 growth, furin-cleavage-site adaptation and neutralization using serum from acutely infected hospitalized COVID-19 patients. *J Gen Virol* (2020).
13. Plante, J.A., et al. Spike mutation D614G alters SARS-CoV-2 fitness. *Nature* (2020).
14. Zhang, L., et al. The D614G mutation in the SARS-CoV-2 spike protein reduces S1 shedding and increases infectivity. *bioRxiv* (2020).
15. Xie, X., et al. An Infectious cDNA Clone of SARS-CoV-2. *Cell host & microbe* **27**, 841-848.e843 (2020).
16. Harcourt, J., et al. Severe Acute Respiratory Syndrome Coronavirus 2 from Patient with 2019 Novel Coronavirus Disease, United States. *Emerg Infect Dis* **26** (2020).
17. Menachery, V.D., et al. Pathogenic influenza viruses and coronaviruses utilize similar and contrasting approaches to control interferon-stimulated gene responses. *mBio* **5**, e01174-01114 (2014).
18. Matsuyama, S., et al. Enhanced isolation of SARS-CoV-2 by TMPRSS2-expressing cells. *Proceedings of the National Academy of Sciences of the United States of America* **117**, 7001-7003 (2020).
19. Imai, M., et al. Syrian hamsters as a small animal model for SARS-CoV-2 infection and countermeasure development. *Proceedings of the National Academy of Sciences of the United States of America* **117**, 16587-16595 (2020).
20. Tostanoski, L.H., et al. Ad26 vaccine protects against SARS-CoV-2 severe clinical disease in hamsters. *Nature medicine* (2020).
21. Bos, R., et al. Ad26 vector-based COVID-19 vaccine encoding a prefusion-stabilized SARS-CoV-2 Spike immunogen induces potent humoral and cellular immune responses. *npj Vaccines* **5**, 91 (2020).
22. Winkler, E.S., et al. SARS-CoV-2 infection of human ACE2-transgenic mice causes severe lung inflammation and impaired function. *Nature immunology* **21**, 1327-1335 (2020).
23. Muruato, A.E., et al. A high-throughput neutralizing antibody assay for COVID-19 diagnosis and vaccine evaluation. *Nature communications* **11**, 4059 (2020).
24. Santiana, M., et al. Vesicle-Cloaked Virus Clusters Are Optimal Units for Inter-organismal Viral Transmission. *Cell host & microbe* **24**, 208-220.e208 (2018).
25. Rivera-Serrano, E.E., González-López, O., Das, A. & Lemmon, S.M. Cellular entry and uncoating of naked and quasi-enveloped human hepatoviruses. *eLife* **8** (2019).
26. Gao, Q., et al. Development of an inactivated vaccine candidate for SARS-CoV-2. *Science* **369**, 77-81 (2020).
27. Hansen, J., et al. Studies in humanized mice and convalescent humans yield a SARS-CoV-2 antibody cocktail. *Science* (2020).

Publisher's note Springer Nature remains neutral with regard to jurisdictional claims in published maps and institutional affiliations.

© The Author(s), under exclusive licence to Springer Nature Limited 2021

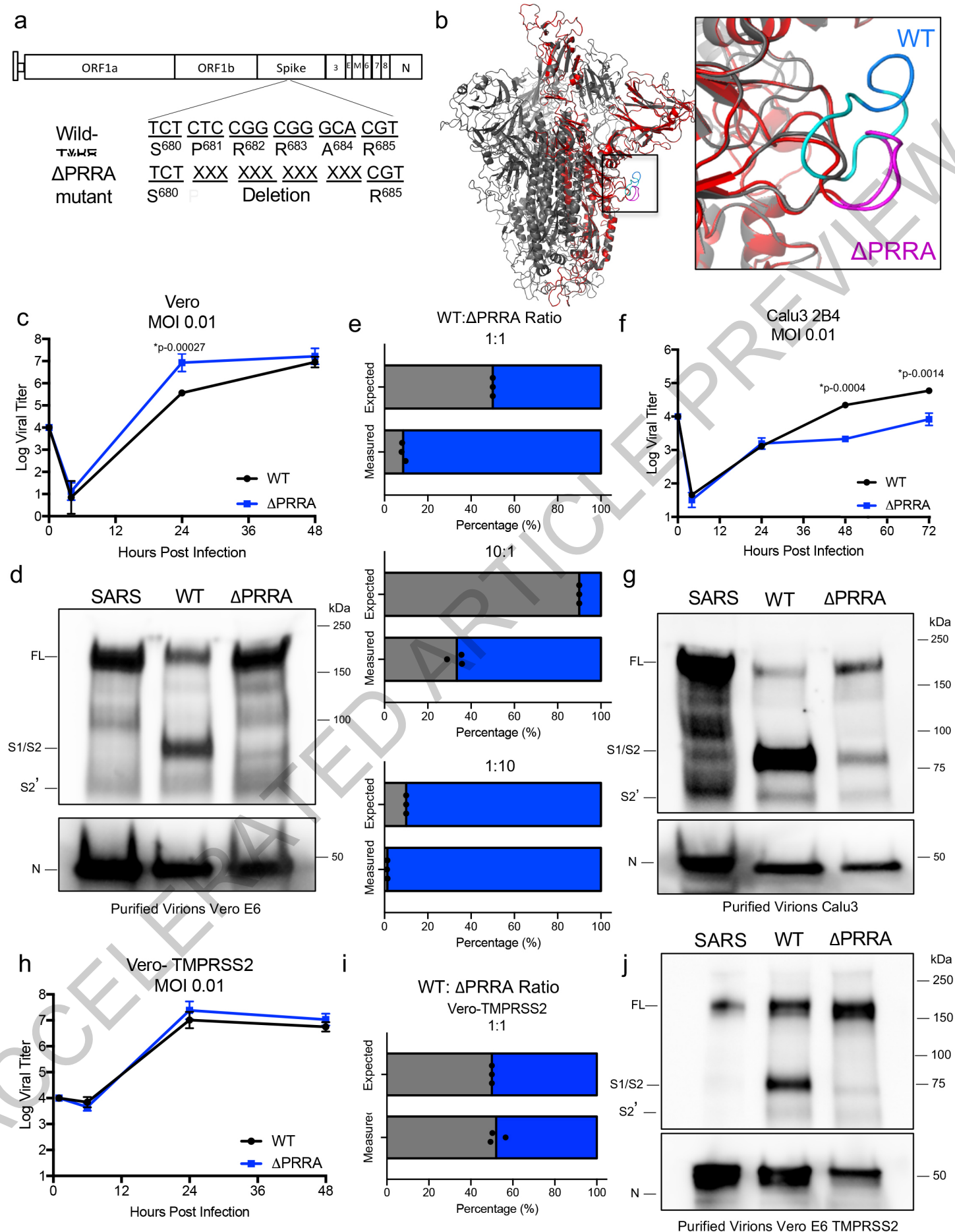


Fig. 1 | See next page for caption.

Fig. 1 | Distinct replication, spike cleavage, and competition for Δ PRRA. a) SARS-CoV-2 schematic to delete the furin cleavage site. b) SARS-CoV-2 trimer (grey) with PRRA deletion mutant monomer overlaid (red). The loop (inset) shows WT SARS-CoV-2 (cyan) with the PRRA sequence (blue) and PRRA deletion mutant (pink). Models were generated using SARS-CoV structure (PDB 6ACD). c) Viral titer from Vero E6 cells infected with WT SARS-CoV-2 (black) or Δ PRRA (blue) at MOI 0.01 (N=3). d) Purified SARS-CoV, SARS-CoV-2 WT, and Δ PRRA virions from Vero E6 cells probed with anti-spike (Top panel) or anti-nucleocapsid antibody (lower panel). Full length (FL), S1/S2 cleavage form, and S2' annotated. Results representative of two independent experiments. e) Competition assay between SARS-CoV-2 WT (black) and Δ PRRA (blue) showing RNA percentage based on quantitative RT-PCR at 50:50, 90:10, and 10:90 WT/ Δ PRRA ratio (N=3 per group). f) Viral titer from Calu3 2B4 cells infected with

WT SARS-CoV-2 (black) or Δ PRRA (blue) at MOI 0.01 (N=3). g) Purified SARS-CoV, SARS-CoV-2 WT, and Δ PRRA virions from Calu3 2B4 cells probed with anti-spike (top panel) or anti-nucleocapsid antibody (lower panel). Results representative of two independent experiments. h) Viral titer from Vero E6 cells expressing TMPRSS2 infected with WT SARS-CoV-2 (black) or Δ PRRA (blue) at MOI 0.01 (N=5). i) Competition assay between SARS-CoV-2 WT (black) and Δ PRRA (blue) on Vero E6 cells expressing TMPRSS2 showing RNA percentage based on quantitative RT-PCR at 50:50 WT/ Δ PRRA ratio (N=3 per group). j) Purified SARS-CoV, SARS-CoV-2 WT, and Δ PRRA virions from Vero E6 cells expressing TMPRSS2 probed with anti-spike (Top) or anti-nucleocapsid antibody (lower). Results representative of two independent experiments. Data presented as mean values +/- SD in c, e, f, h and i. P-values based on a two-tailed Student T-test.

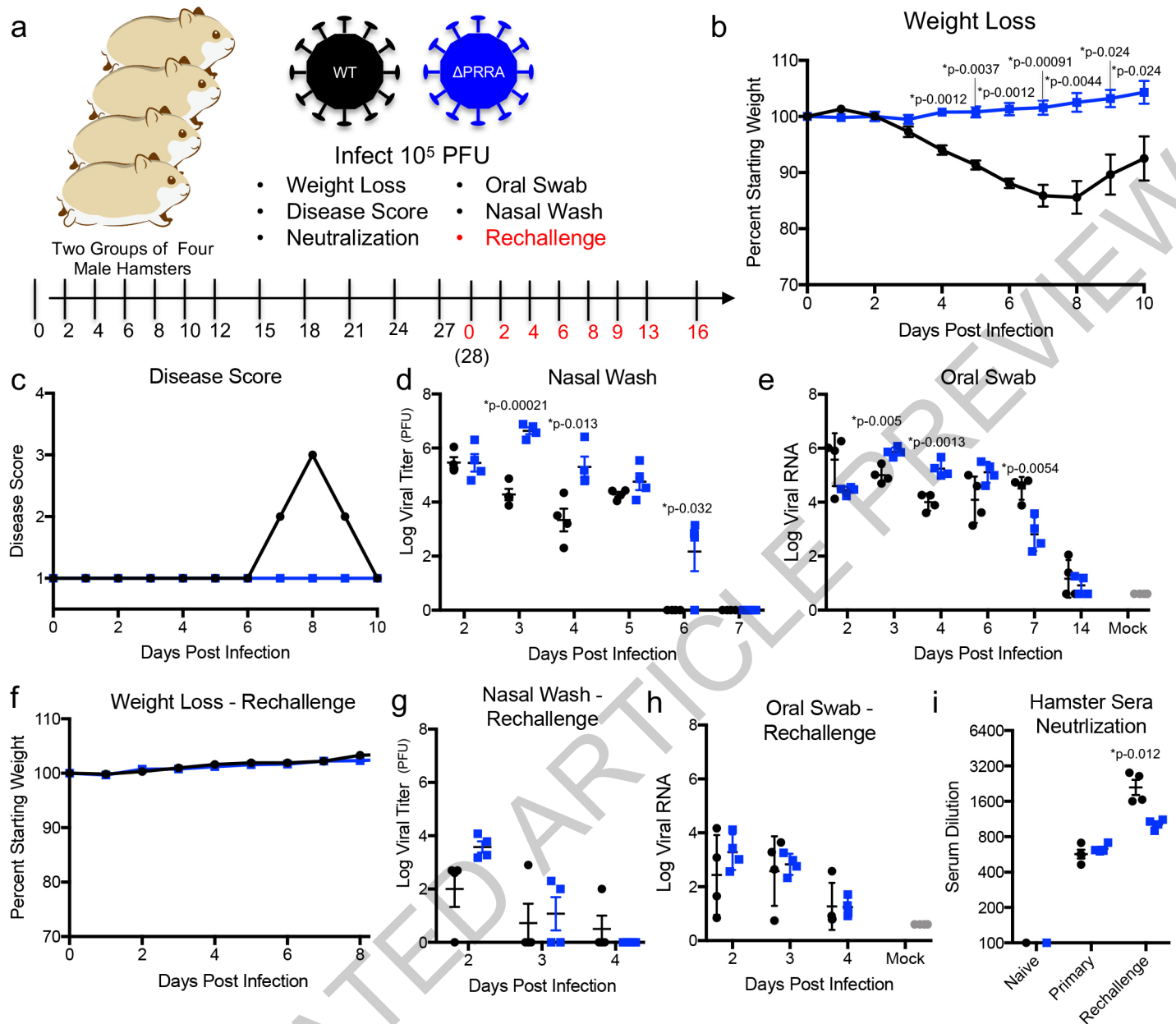


Fig. 2 | Hamster infections with Δ PRRA mutant. a, Primary SARS-CoV-2 challenge schematic. Two groups of male hamsters (N=4) were challenged with 10^5 plaque forming units (PFU) of either SARS-CoV-2 WT or Δ PRRA mutant and evaluated (b) weight loss, (c) disease score, (d) viral titer from nasal wash and (e) viral RNA from oral swabs. f-k, Twenty eight DPI, hamsters infected with

SARS-CoV-2 WT or Δ PRRA were rechallenged with 10^5 PFU of SARS-CoV-2 WT and evaluated for (f) weight loss, (g) viral titer from nasal wash, (h) viral RNA from oral swabs, and (i) PRNT50 dilution from primary and rechallenge hamster sera. Data presented as mean values \pm SEM. P-values based on a two-tailed Student T-test.

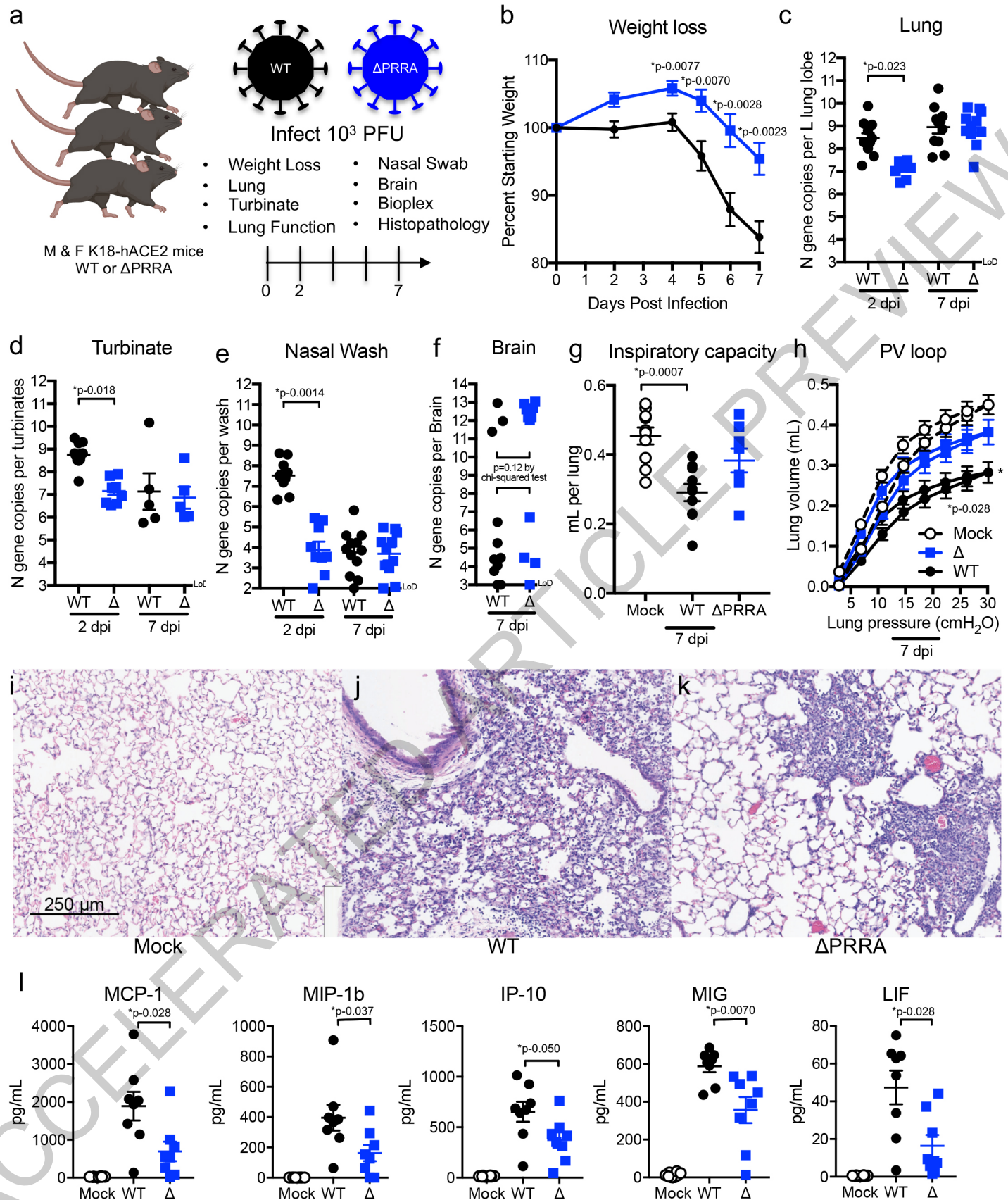


Fig. 3 | Infection of K18-hACE2 transgenic mice with Δ PRRA mutant. a, SARS-CoV-2 challenge schematic created with BioRender. Male and female mice were challenged with 10^3 PFU of SARS-CoV-2 WT (black) or Δ PRRA mutant (blue) and evaluated for (b) weight loss (N=12 for both groups), viral RNA from the (c) lung (d) nasal turbinate, (e) nasal wash, and (f) brain. N=9 for WT and 11 Δ PRRA D2, N=11 for both at D4. g-h, Lung function evaluated using Flexivent mechanical ventilator to assess (g) inspiratory capacity, and (h) pressure/volume (PV) loop. N=10 for WT and

9 for Δ PRRA. i-k, Lung histopathology 7 DPI from (i) mock, (j) WT and (k) Δ PRRA infected mice. Images represent lung sections from 3 mock, 3 WT, and 3 of Δ PRRA infected mice. l, Chemokine analysis of mouse lung homogenates at 7 DPI with mock (open), WT (black), or Δ PRRA SARS-CoV-2 (blue). N=8 for all groups. Data are presented as mean values \pm SEM. Scale bar represents 250 μ m for (i-k). P-values based on a two-tailed Student T-test with unequal variance (b), Kruskal-Wallis Test for multiple comparisons (c-k) or a two-tailed Mann-Whitney test between WT and Δ PRRA (l).

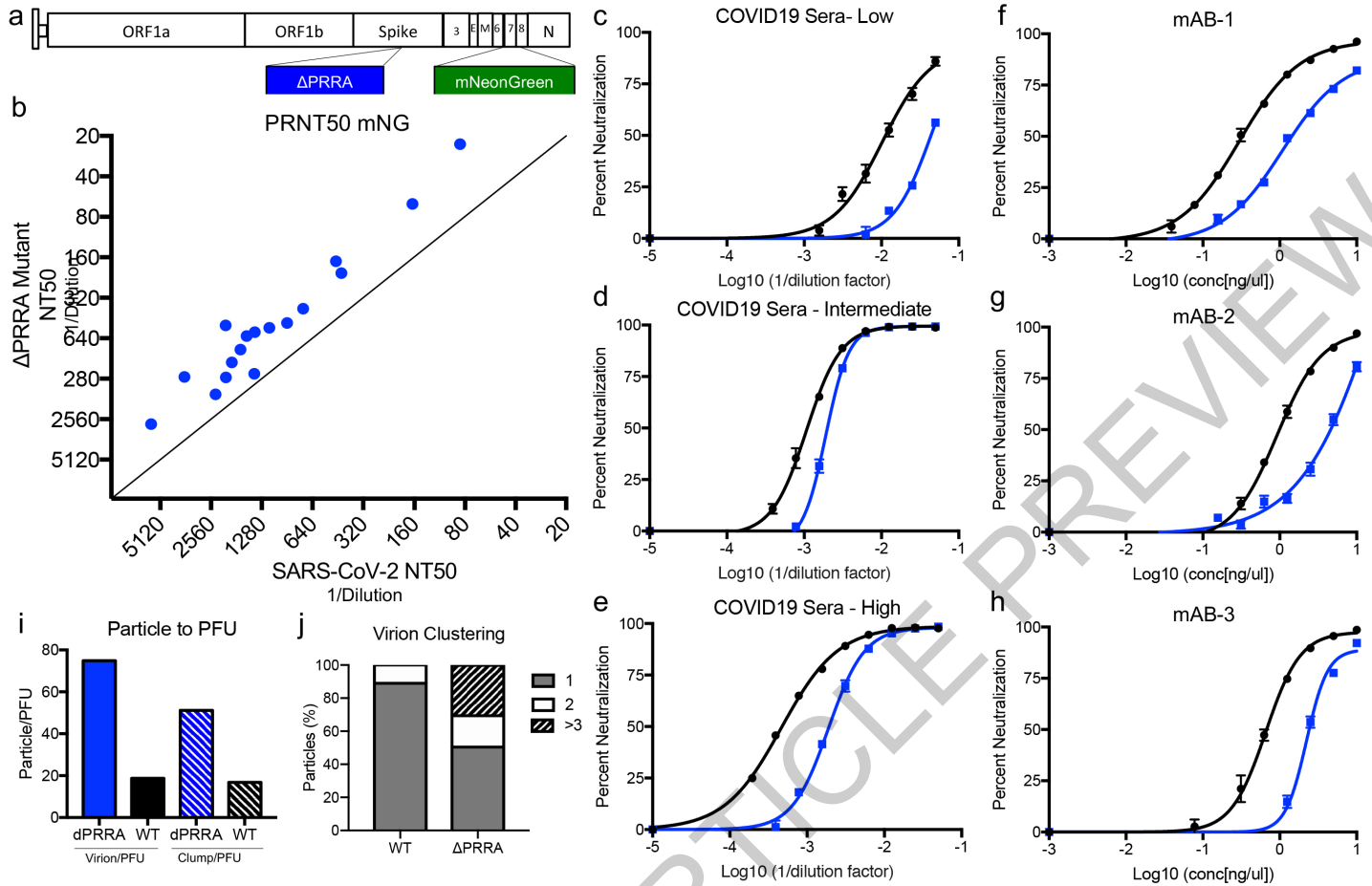


Fig. 4 | Accessing antibody neutralization of Δ PRRA mutant. a) Schematic for SARS-CoV-2 Δ PRRA reporter virus expressing mNeonGreen (mNG) gene in place of ORF7. b) Plaque reduction neutralization (PRNT50) values measured mNG expression. PRNT50 values plotted as Log (1/serum dilution) with Δ PRRA on Y axis and WT on the X axis. c-e) Representative curves from c) low, d) intermediate, and e) high neutralizing COVID-19 patient sera. N=3. f-h) Neutralization curves from mAB-1 (f), mAB-2 (g), and mAB-3 (h), N=3. i) Particle/PFU ratio determined from 40 fields dividing into individual particle (left) and clusters to determine ratio. j) Percentage of particles as individual virions (1), doubles (2) or larger clusters (>3). Data are presented as mean values \pm SEM.

Article

Methods

Viruses and cells

The recombinant wild-type and mutant SARS-CoV-2 are based on the sequence of USA-WA1/2020 isolate provided by the World Reference Center for Emerging Viruses and Arboviruses (WRCEVA) and was originally obtained from the USA Centers for Disease Control and Prevention as described¹⁶. Wild-type and mutant SARS-CoV-2 as well as recombinant mouse-adapted recombinant SARS-CoV²⁸ were titrated and propagated on Vero E6 cells or Vero E6 cells expressing TMPRSS2 (Sekisui XenoTech, Kansas City, KS), grown in DMEM with 5% fetal bovine serum and 1% antibiotic/antimycotic (Gibco). Calu3 2B4 cells were grown in DMEM with 10% defined fetal bovine serum, 1% sodium pyruvate (Gibco), and 1% antibiotic/antimycotic (Gibco). Standard plaque assays were used for SARS-CoV and SARS-CoV-2^{29,30}. All experiments involving infectious virus were conducted at the University of Texas Medical Branch (Galveston, TX), Emory University (Atlanta, Georgia), or Washington University (St. Louis, Missouri) in approved biosafety level 3 (BSL) laboratories with routine medical monitoring of staff.

Construction of Δ PRRA mutant viruses

Both wild-type and mutant viruses were derived from the SARS-CoV-2 USA-WA1/2020 infectious clone as previously described¹⁵. For Δ PRRA construction, the mutation was introduced into a sub-clone puc57-CoV2-F6 by using overlap PCR with primers Δ PRRA-F (5'-GACTAATTCTCGTAGTGTAGCTAGTCAATCCATC-3') and Δ PRRA-R (5'-GACTAGTACTACTACGAGAATTAGTCTGAGTC-3'). The resulted plasmid was validated by restriction enzyme digestion and Sanger sequencing. Thereafter, plasmids containing wild-type and mutant SARS-CoV-2 genome fragments were amplified and digested by restriction enzyme. The SARS-CoV-2 genome fragments were purified and ligated *in vitro* to assemble the full-length cDNA according to the procedures described previously¹⁵. *In vitro* transcription reactions then were performed to synthesize full-length genomic RNA. To recover the viruses, the RNA transcripts were electroporated into Vero E6 cells. The medium from electroporated cells as harvested at 40 HPI and served as seed stocks for subsequent experiments. Viral mutants were confirmed by sequence analysis prior to use. Synthetic construction of SARS-CoV-2 Δ PRRA mutant was approved by the University of Texas Medical Branch Institutional Biosafety Committee.

In vitro infection

Viral infections in Vero E6 and Calu3 2B4 cells were performed as previously described^{31,32}. Briefly, cells were washed with PBS and inoculated with SARS-CoV or SARS-CoV-2 at a multiplicity of infection (MOI) 0.01 for 60 min at 37 °C. Following inoculation, cells were washed, and fresh media was added to signify time 0. Three or more biological replicates were harvested at each described time. No blinding was used in any sample collections, nor were samples randomized. Microsoft Excel for Mac 2011 was used to analyze data.

Virion purification and Western blotting

Vero E6 or Calu3-2B4 cells were infected with WT or PRRA mutant viruses at an MOI of 0.01. At 24 or 48 HPI, the culture medium was collected and clarified by low speed centrifugation. Virus particles in the supernatant were subsequently pelleted by ultracentrifugation through a 20% sucrose cushion at 26,000 rpm for 3 h using a Beckman SW28 rotor. Protein lysates were prepared from the pellets using 2X Laemmli Sample buffer (Cat# 161-073, BioRad, Hercules, Ca). Relative viral protein levels were determined by SDS-PAGE followed by Western blot analysis as previously described^{16,33}. Briefly, sucrose purified SARS-CoV, SARS-CoV-2, and SARS-CoV-2 Δ PRRA inactivated by boiling in Laemmli Buffer. Samples were loaded in equal volumes into 4-20% Mini-PROTEAN TGX Gels (Biorad# 4561093) and electrophoresed by

SDS-PAGE. Protein was transferred to polyvinylidene difluoride (PVDF) membranes. Membranes were blotted with SARS-CoV Spike (S) specific antibodies (Novus Biologicals #NB100-56578), followed by probing with horseradish peroxidase (HRP)-conjugated anti-rabbit antibody (Cell Signaling Technology #7074S). Blots were stripped and re-probed with SARS-CoV Nucleocapsid (N) specific antibodies (provided as a kind gift from Dr. Shinji Makino) and the HRP-conjugated anti-rabbit secondary IgG. In both cases, signal was developed by treating membranes with Clarity Western ECL substrate (Bio-Rad #1705060) imaging on a ChemiDoc MP System (Bio-Rad #12003154). Densitometry was performed using ImageLab 6.0.1 (Bio-Rad #12012931).

Competition assay and Real-Time PCR

For competition assays, ratios (50:50, 90:10, 10:90 WT/ Δ PRRA) were determined by PFU derived from viral stocks. Vero cells were infected at MOI 0.1 (WT+ Δ PRRA) as described above. RNA from cell lysates were collected using Trizol reagent (Invitrogen). RNA was then extracted from Triazol using the Direct-zol RNA Miniprep Plus kit (Zymo Research #R2072) per the manufacturer's instruction. Extracted RNA was then converted to cDNA with the iScript cDNA Synthesis kit (BioRad #1708891). Quantitative real time PCR (qRT-PCR) was performed with the Luna Universal qPCR Master Mix (New England Biolabs #M3003) on a CFX Connect instrument (BioRad #1855200). For differentiation between wild type SARS-CoV-2 and SARS-CoV-2 Δ PRRA genomes in competition experiments, Primer 1 (Forward - AAT GTT TTT CAA ACA CGT GCA G and Primer 2 (Reverse - TAC ACT ACG TGC CCG CCG AGG) were used to detect wild type genomes only. For detecting total genomes, Primer 1 and Primer 3 (Reverse - GAA TTT TCT GCA CCA AGT GAC A) were used. 8-point standard curves (1×10^1 to 1×10^8 copies/ μ L) were utilized to quantify the signal. A primer annealing temperature of 63 °C was used for all assays.

For detection of viral RNA the nasal washes and oral swabs of SARS-CoV-2 and SARS-CoV-2 Δ PRRA infected hamsters, RNA extraction, cDNA synthesis, and qRT-PCR were performed as described above. For qRT-PCR, Primer 1 and Primer 3 were utilized for all hamster samples.

Deep sequencing analysis

RNA libraries were prepared with 300 ng of RNA using the Click-Seq protocol as previously described³⁴ using tiled primers cognate to the SARS-COV-2 genome (accession number NC_045512.2) and the TruSeq i7 LT adapter series and i5 hexamer adaptors containing a 12N unique molecular identifier (UMI). Libraries were sequenced on the Illumina MiSeq platform with MiSeq Reagent Kit v2. Raw data was de-multiplexed using TruSeq indexes using the MiSeq Reporter Software. Fastp v0.12.35 was used to trim adapter sequences and low-quality reads ($q < 25$), remove reads less than 40 nts in length, and copy UMI sequences onto the read name. Reads were aligned with bowtie using the -best parameter and allowing for up to two mismatches. The alignment index was generated from a single fasta file, which contained two 600nt reference sequences spanning the PRRA locus (23603-23616) of the wildtype (accession number NC_045512.2) and Δ PRRA genomes. The alignments were sorted and indexed using Samtools v1.9³⁶, PCR duplicates were removed using umi_tools³⁷. Coverage at each position was determined with the genomecov function in bedtools v2.25.0³⁸.

Plaque reduction neutralization test

Neutralization assays were performed using mNeonGreen SARS-CoV-2 reporter neutralization assay as previously described²³. Briefly, Vero E6 cells were plated black μ CLEAR flat-bottom 96-well plate (Greiner Bio-one™). On following day, sera or monoclonal antibodies were serially diluted from 1/20 with nine 2-fold dilutions to the final dilution of 1/5120 and incubated with mNeonGreen SARS-CoV-2 or Δ PRRA expressing mNeonGreen at 37 °C for 1 h. The virus-serum mixture was transferred to the Vero E6 cell plate with a final MOI of 0.5. After 20 h, Hoechst 33342 Solution (400-fold diluted in Hank's Balanced Salt

Solution; Gibco) was added to stain cell nucleus, sealed with Breath-Easy sealing membrane (Diversified Biotech), incubated at 37 °C for 20 min, and quantified for mNeonGreen fluorescence on Cytation™ 7 (BioTek). The raw images (2×2 montage) were acquired using 4× objective, processed, and stitched using the default setting. The total cells (indicated by nucleus staining) and mNeonGreen-positive cells were quantified for each well. Infection rates were determined by dividing the mNeonGreen-positive cell number to total cell number. Relative infection rates were obtained by normalizing the infection rates of serum-treated groups to those of non-serum-treated controls. The curves of the relative infection rates versus the serum dilutions (log₁₀ values) were plotted using Prism 8 (GraphPad). A nonlinear regression method was used to determine the dilution fold that neutralized 50% of mNeonGreen fluorescence (NT50). Each serum was tested in duplicates.

Phylogenetic tree, sequence identity heat map, and structural modeling

Heat maps were constructed from a set of representative group 2B coronaviruses by using alignment data paired with neighbor-joining phylogenetic trees built in Geneious (v.9.1.5) using the spike amino acid sequences derived the following accession numbers: QHU79204 (SARS-CoV-2 WA1), QHR63300.2 (RATG13), QND76034.1 (HKU3), AGZ48828.1 (WIV1), AGZ48806 (RsSHC014), ALK02457 (WIV16), and AYW99817.1(SARS-CoV Urbani). Sequence identity was visualized using EvolView (<http://evolgenius.info/>) and SARS-CoV Co-V-2 WA1 served as the reference sequence. Structural models were generated using SWISS-Model^{39,40} to generate homology models for SARS-CoV-2 spike with and without the furin cleavage site based on the SARS-CoV-1 trimer structure (PDB 6ACD). Homology models were visualized and manipulated in MacPyMol (version 1.3).

Transmission Electron Microscopy (TEM)

Supernatants of SARS-CoV-2 infected cells were centrifuged for 10 min at 3,000 g to remove large cellular debris. Nickel grids were incubated with clarified supernatants for 10 min followed by glutaraldehyde fixation and 2% uranyl acetate staining. Micrographs were taken using a JEM 14000 (JEOL USA Inc.). Multiple randomly selected fields were imaged to obtain unbiased particle counts.

Hamster infection studies

Male Syrian hamsters (7-8 weeks old, 86–127 g) were purchased from Envigo. All procedures were conducted under an animal protocol approved by the UTMB Institutional Animal Care and Use Committee and complied with USDA guidelines in an AAALAC-accredited lab. Work with infectious SARS-CoV-2 in hamsters was performed in the Galveston National Laboratory BSL-4 laboratory. Animals were housed in microisolator caging equipped with HEPA filters in the BSL-4 laboratories. Hamsters were challenged with 10⁵ PFU of WT-SARS-CoV-2 or SARS-CoV-2 ΔPRRA by intranasal inoculation (i.n.). Hamsters were observed daily for the development of clinical disease and body weights were taken every day for the first 10 days of the study, then every third day. For each manipulation (viral infection, retro-orbital bleeds, nasal wash, or oral swab), animals were anesthetized with isoflurane (Piramal, Bethlehem, PA).

Mouse infection studies

Mouse studies were carried out in accordance with the recommendations in the Guide for the Care and Use of Laboratory Animals of the National Institutes of Health. The protocols were approved by the Institutional Animal Care and Use Committee at the Washington University School of Medicine (assurance number A3381–01) and performed in an ABSL3 facility. Heterozygous K18-hACE2 C57BL/6J mice (strain: 2B6. Cg-Tg(K18-ACE2)2PrImn/J) were obtained from The Jackson Laboratory and randomized to upon arrival. Animals were housed in 7.5×11.5×5" cages in groups of ≤5 and fed standard chow diets (PicoLab Rodent

Diet 5053, Purina). Cages were changed weekly. The ABSL-3 room was kept between 68-74 degrees Fahrenheit with 30-60% and 12h-12h light cycles (6AM-6PM). Mice of both sexes were used for experimentation. Animals were housed in groups of ≤5 individuals in rooms maintained between 20.0-23.3oC with 30-60% humidity. Mice were given *ad libitum* access to water and PicoLab Rodent Diet 5053 chow (Purina). Virus inoculations were performed under anesthesia that was induced and maintained with ketamine hydrochloride and xylazine; all efforts were made to minimize animal suffering. Mice of different ages (5-9 weeks old) and both sexes were administered 10³ PFU of SARS-CoV-2 in a 50 μL intranasal dose.

Cytokine and chemokine protein measurements

Lung homogenates were incubated with Triton-X-100 (1% final concentration) for 1 h at room temperature to inactivate SARS-CoV-2. Homogenates then were analyzed for cytokines and chemokines by Eve Technologies Corporation (Calgary, AB, Canada) using their Mouse Cytokine Array/Chemokine Array 31-Plex (MD31) platform.

Respiratory mechanics

Mice were anesthetized with ketamine/xylazine (100 mg/kg and 10 mg/kg, i.p., respectively). The trachea was isolated via dissection of the neck area and cannulated using an 18-gauge blunt metal cannula (typical resistance of 0.18 cmH₂O.s/mL), which was secured in place with a nylon suture. The mouse then was connected to the flexiVent computer-controlled piston ventilator (SCIREQ Inc.) via the cannula, which was attached to the FX adaptor Y-tubing. Mechanical ventilation was initiated, and mice were given an additional 100 mg/kg of ketamine and 0.1 mg/mouse of the paralytic pancuronium bromide via intraperitoneal route to prevent breathing efforts against the ventilator and during measurements. Mice were ventilated using default settings for mice, which consisted in a positive end expiratory pressure at 3 cm H₂O, a 10 mL/kg tidal volume (Vt), a respiratory rate of 150 breaths per minute (bpm), and a fraction of inspired oxygen (FiO₂) of 0.21 (i.e., room air). Respiratory mechanics were assessed using the forced oscillation technique, as previously described⁴¹, using the latest version of the FlexiVent operating software (FlexiWare v8.1.3). Pressure-volume loops and measurements of inspiratory capacity were also performed.

Measurement of viral burden

Mouse tissues were weighed and homogenized with zirconia beads in a MagNA Lyser instrument (Roche Life Science) in 1000 μL of DMEM media supplemented with 2% heat-inactivated FBS. Tissue homogenates were clarified by centrifugation at 10,000 rpm for 3 min and RNA was extracted from 50 μL of supernatant using the MagMax mirVana Total RNA isolation kit (Thermo Scientific) on the Kingfisher Flex extraction robot (Thermo Scientific). RNA was reverse transcribed and amplified using the TaqMan RNA-to-CT 1-Step Kit (ThermoFisher). Reverse transcription was carried out at 48 °C for 15 min followed by 2 min at 95 °C. Amplification was accomplished over 50 cycles as follows: 95 °C for 15 s and 60 °C for 1 min. Copies of SARS-CoV-2 N gene RNA in samples were determined using a previously published assay. Briefly, a TaqMan assay was designed to target a highly conserved region of the N gene (Forward primer: ATGCTGCAATCGTGCTACAA; Reverse primer: GACTGCCGCCTCTGCTC; Probe: /56-FAM/TCAAGGAAC/ZEN/AACATTGCCAA/3IABkFQ/). This region was included in an RNA standard to allow for copy number determination down to 10 copies per reaction. The reaction mixture contained final concentrations of primers and probe of 500 and 100 nM, respectively.

Histology and RNA in situ hybridization

Upon euthanasia, the lung was inflated with -1.2 mL of 10% neutral buffered formalin using a 3-mL syringe and catheter inserted into the trachea. The airway, lungs, and heart were removed en bloc and transferred to a conical containing 40 mL 10% neutral buffered formalin,

Article

where the tissues were allowed to fix for suspension of neutral buffered formalin for ≥ 7 days. Tissues were embedded in paraffin, and sections were stained with hematoxylin and eosin by the Washington University Lung Morphology Core. Images were captured using the Nanozoomer (Hamamatsu) at the Alafi Neuroimaging Core at Washington University.

Biological Materials

Recombinant wild-type and mutant SARS-CoV-2 described in this manuscript will be made available through the World Reference Center for Emerging Viruses and Arboviruses (WRCEVA) at UTMB through material transfer agreement.

Reporting summary

Further information on research design is available in the Nature Research Reporting Summary linked to this paper.

Data availability

The raw data that support the findings of this study are available from the corresponding author upon reasonable request.^{42–45} Source data are provided with this paper.

28. Harcourt, J., et al. Severe Acute Respiratory Syndrome Coronavirus 2 from Patient with 2019 Novel Coronavirus Disease, United States. *Emerg Infect Dis* **26** (2020).
29. Roberts, A., et al. A mouse-adapted SARS-coronavirus causes disease and mortality in BALB/c mice. *PLoS pathogens* **3**, e5 (2007).
30. Sims, A.C., et al. Release of severe acute respiratory syndrome coronavirus nuclear import block enhances host transcription in human lung cells. *J Virol* **87**, 3885–3902 (2013).
31. Josset, L., et al. Cell host response to infection with novel human coronavirus EMC predicts potential antivirals and important differences with SARS coronavirus. *MBio* **4**, e00165–00113 (2013).
32. Xie, X., et al. An Infectious cDNA Clone of SARS-CoV-2. *Cell host & microbe* **27**, 841–848 e843 (2020).
33. Sheahan, T., Rockx, B., Donaldson, E., Corti, D. & Baric, R. Pathways of cross-species transmission of synthetically reconstructed zoonotic severe acute respiratory syndrome coronavirus. *Journal of virology* **82**, 8721–8732 (2008).
34. Menachery, V.D., et al. Attenuation and restoration of severe acute respiratory syndrome coronavirus mutant lacking 2'-O-methyltransferase activity. *Journal of virology* **88**, 4251–4264 (2014).
35. van Tol, S., et al. VAMP8 Contributes to the TRIM6-Mediated Type I Interferon Antiviral Response during West Nile Virus Infection. *Journal of virology* **94** (2020).
36. Routh, A., Head, S.R., Ordoukhanian, P. & Johnson, J.E. ClickSeq: Fragmentation-Free Next-Generation Sequencing via Click Ligation of Adaptors to Stochastically Terminated 3'-Azido cDNAs. *J Mol Biol* **427**, 2610–2616 (2015).

37. Chen, S., Zhou, Y., Chen, Y. & Gu, J. fastp: an ultra-fast all-in-one FASTQ preprocessor. *Bioinformatics* **34**, i884–i890 (2018).
38. Li, H., et al. The Sequence Alignment/Map format and SAMtools. *Bioinformatics* **25**, 2078–2079 (2009).
39. Smith, T., Heger, A. & Sudbery, I. UMI-tools: modeling sequencing errors in Unique Molecular Identifiers to improve quantification accuracy. *Genome Res* **27**, 491–499 (2017).
40. Quinlan, A.R. & Hall, I.M. BEDTools: a flexible suite of utilities for comparing genomic features. *Bioinformatics* **26**, 841–842 (2010).
41. Murato, A.E., et al. A high-throughput neutralizing antibody assay for COVID-19 diagnosis and vaccine evaluation. *Nature communications* **11**, 4059 (2020).
42. Waterhouse, A., et al. SWISS-MODEL: homology modelling of protein structures and complexes. *Nucleic Acids Res* **46**, W296–W303 (2018).
43. Bienert, S., et al. The SWISS-MODEL Repository—new features and functionality. *Nucleic Acids Res* **45**, D313–D319 (2017).
44. McGovern, T.K., Robichaud, A., Fereydoonzad, L., Schuessler, T.F. & Martin, J.G. Evaluation of respiratory system mechanics in mice using the forced oscillation technique. *J Vis Exp*, e50172 (2013).
45. Gralinski, L.E., et al. Mechanisms of Severe Acute Respiratory Syndrome Coronavirus-Induced Acute Lung Injury. *mBio* **4** (2013).

Acknowledgements Research was supported by grants from NIA and NIAID of the NIH to (AI153602 and AG049042 to VDM AI142759, AI134907, AI145617, and UL1TR001439 to P-YS; R01AI123449 to AF and BL; R24AI120942 (WRCEVA) to SCW, R01AI157155 and Defense Advanced Research Project Agency (HRO01117S0019) to MSD). Research was also supported by STARS Award provided by the University of Texas System to VDM and trainee funding provided by the McLaughlin Fellowship Fund at UTMB. P-YS was also supported by CDC grant for the Western Gulf Center of Excellence for Vector-Borne Diseases, and awards from the Sealy & Smith Foundation, Kleberg Foundation, John S. Dunn Foundation, Amon G. Carter Foundation, Gilson Longenbaugh Foundation, and Summerfield Robert Foundation.

Author contributions Conceptualization, XX, BAJ, ALR, MS, ANF, P-YS, and VDM; Methodology, BAJ, XX, BK, KGL, DS, ALR, ANF, P-YS and VDM.; Investigation, BAJ, XX, BK, KGL, AM, JZ, XZ, TJ, JKS, LZ, CS, MV, AV, ESW, DS, NB, JAP, ALR, KD, and VDM.; Resources, KSP, SCW, MSS, PR, VP, ZK, ZA, P-YS, MSD, ANF, VDM; Data Curation, BAJ, XX, BK, KGL, AV, ESW, DS, ALR, MSS, KD, P-YS, ANF, VDM.; Writing—Original Draft, VDM; Writing—Review & Editing, BAJ, XX, BL, PA, MSS, KD, VP, ZK, ZA, P-YS, ANF, VDM, MSD, P-YS; Data Visualization, XX, BAJ, ALB, BK, KGL, NB, ANF, VDM; Supervision, PA, SCW, MSS, P-YS, ANF, VDM.; Funding Acquisition, PA, SCW, P-YS, ANF, VDM.

Competing interests XX, P-YS, and VDM have filed a patent on the reverse genetic system and reporter SARS-CoV-2. Other authors declare no competing interests. M.S.D. is a consultant for Inbios, Vir Biotechnology, NGM Biopharmaceuticals, and on the Scientific Advisory Board of Moderna and Immunome. The Diamond laboratory has received unrelated funding support in sponsored research agreements from Moderna, Vir Biotechnology, and Emergent BioSolutions.

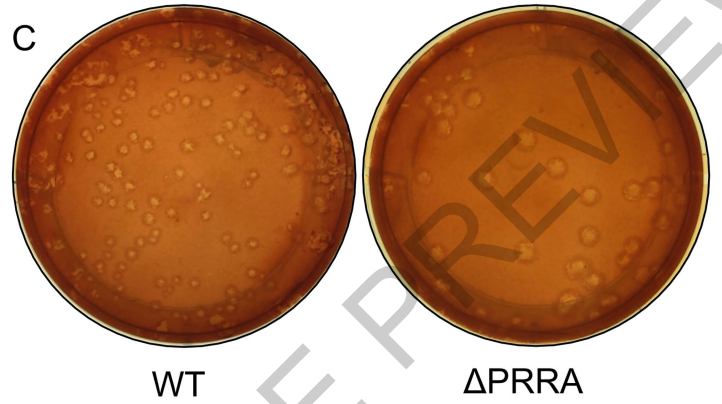
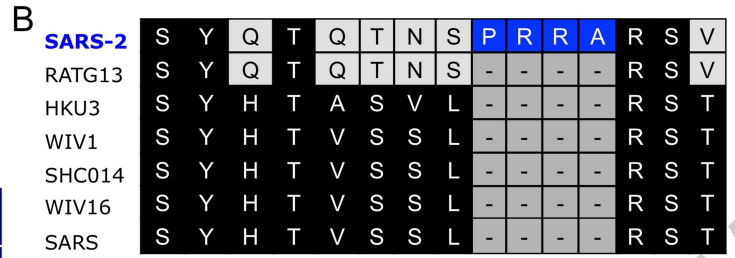
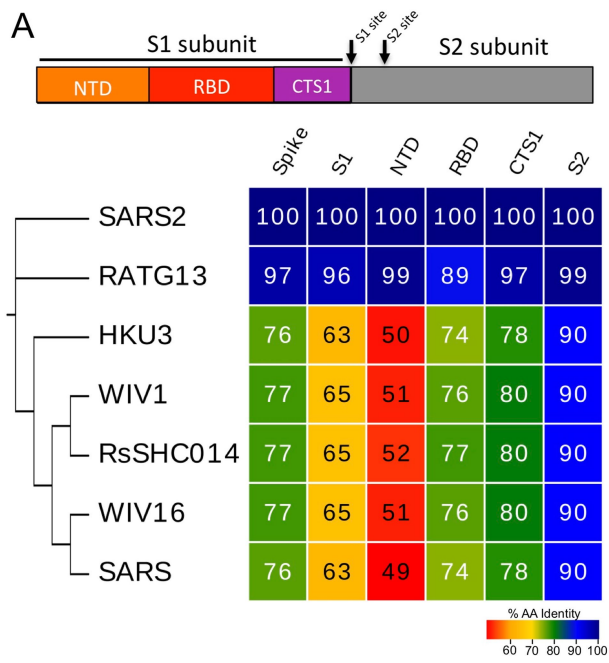
Additional information

Supplementary information The online version contains supplementary material available at <https://doi.org/10.1038/s41586-021-03237-4>.

Correspondence and requests for materials should be addressed to V.D.M.

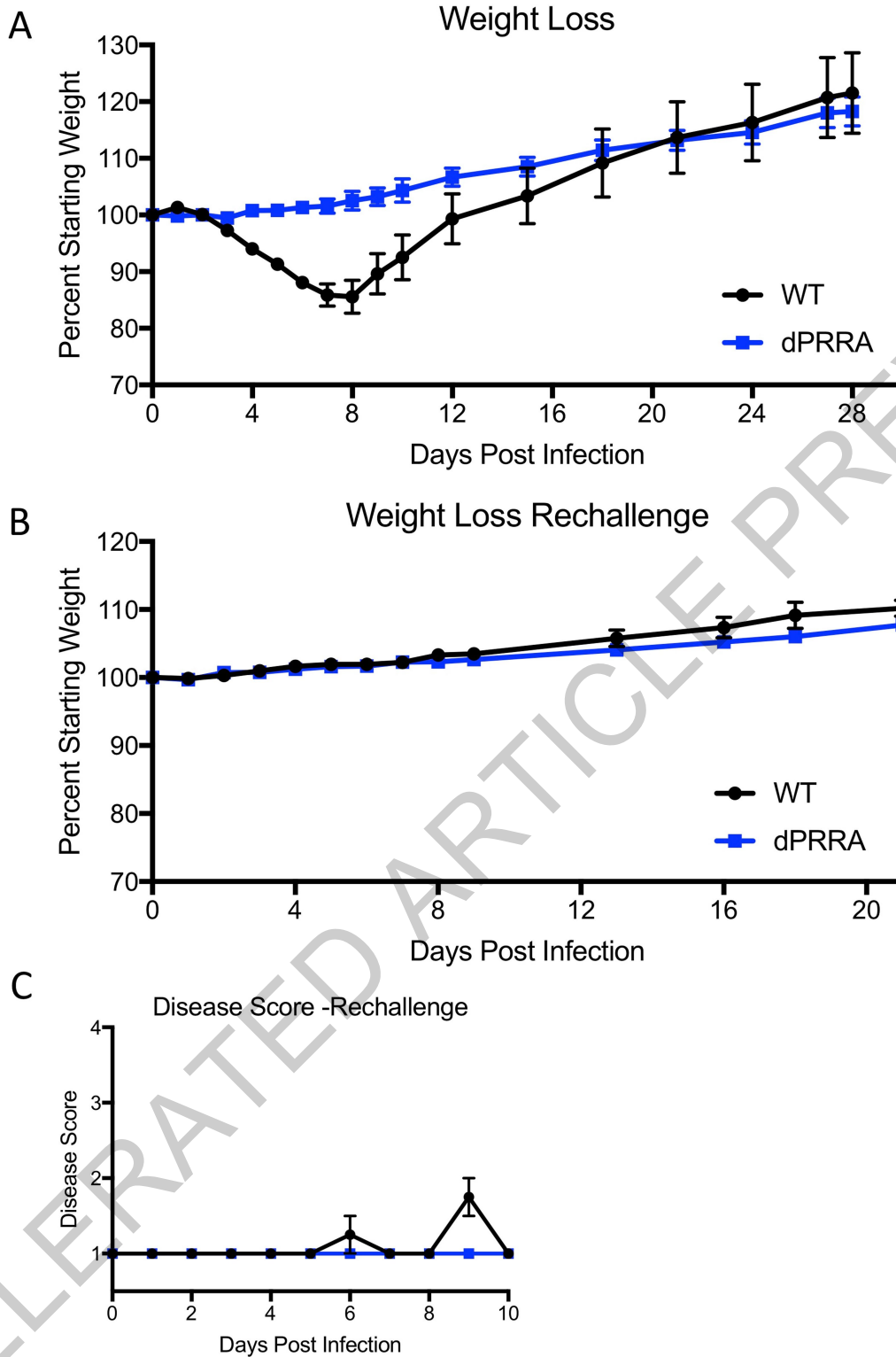
Peer review information Nature thanks the anonymous reviewer(s) for their contribution to the peer review of this work.

Reprints and permissions information is available at <http://www.nature.com/reprints>.



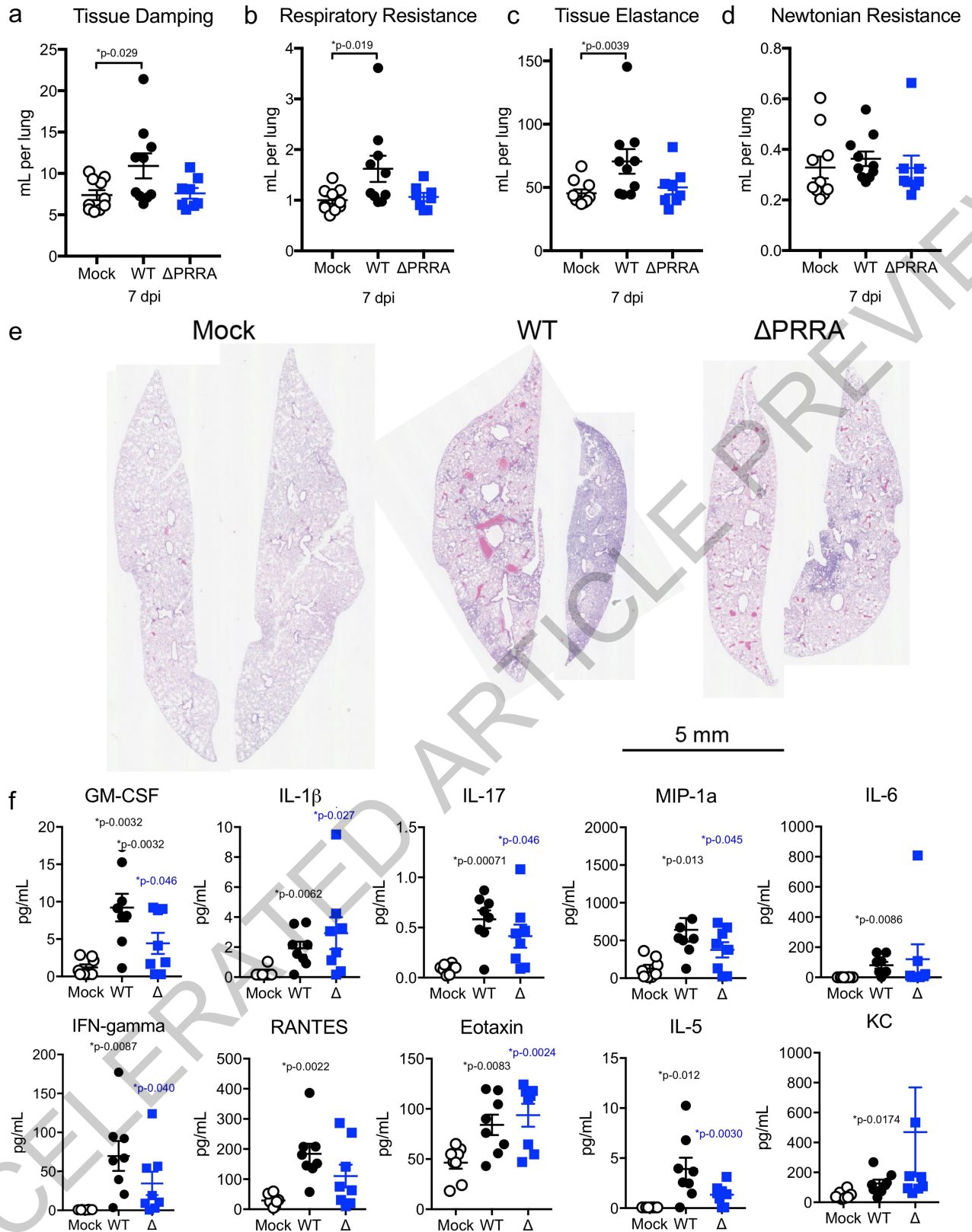
Extended Data Fig. 1 | Furin cleavage site in SARS-CoV-2 spike. A) Diagram of the coronavirus spike protein domains and cleavage sites. The sequences of the indicated group 2B coronaviruses were aligned according to the bounds of total spike, S1, N-terminal domain (NTD), Receptor binding domain (RBD), and C-terminal of S1 (CTS1) and S2. Sequence identities were extracted from the alignments, and a heatmap of sequence identity was constructed using

EvoView (www.evolgenius.info/evolview) with SARS-CoV-2 WA1 as the reference sequence. B) Alignment of the furin cleavage site of SARS-CoV-2 and the corresponding amino acids identities found closely related group 2B CoVs. The PRRA insertion is unique to SARS-CoV-2 C) Representative plaque morphology of WT and ΔPRRA SARS-CoV-2.



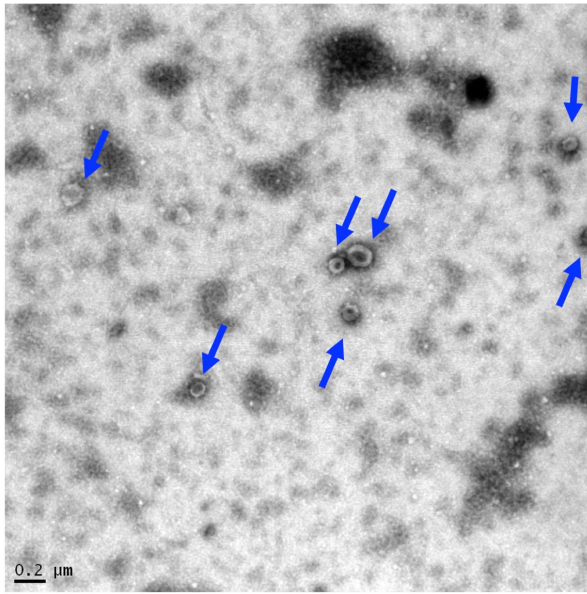
Extended Data Fig. 3 | *In vivo* attenuation of Δ PRRA mutant. a) Weight loss following primary WT and Δ PRRA mutant SARS-CoV-2 challenge (N=4 per group). b & c) Weight loss (b) and disease score (c) following rechallenge of WT

and Δ PRRA mutant infected mice with WT SARS-CoV-2 (N=4 per group). Data are presented as mean values \pm SEM.

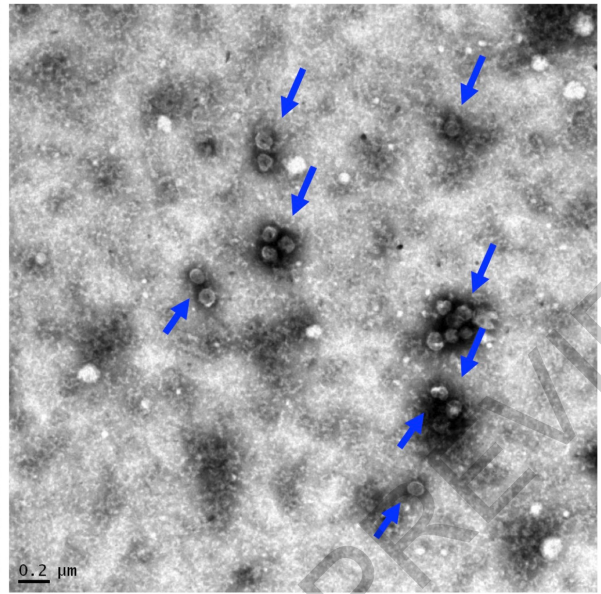


Extended Data Fig. 4 | *In vivo* attenuation of Δ PRRA mutant in K18-hACE2 mice. a-d) Lung function evaluated using flexivent for a) tissue damping, b) respiratory resistance c) tissue elastance, and d) Newtonian resistance. (a-d) N=10 for WT and 8 for Δ PRRA. E) Whole lung histopathology sections seven days post infection from I) mock, J) WT and K) Δ PRRA infected mice with least (left) and most (right) severe sections as representative samples from 3 mock, 2

WT, and 3 Δ PRRA infected mice F) Chemokine/cytokine analysis of mouse lung seven days post infection with mock (open), WT (black), or Δ PRRA SARS-CoV-2. N=8 for all groups. P-values based on a two-tailed Mann-Whitney (a-d) or a two-tailed student T-test (f) relative to control. Data are presented as mean values +/-SEM. Scale bar represents 5mm.



SARS-CoV-2 WT



SARS-CoV-2 ΔPRRA

Extended Data Fig. 5 | ΔPRRA Virion Morphology and Clumping.

Transmission electron microscopy of WT (left) and ΔPRRA (right) SARS-CoV-2 with arrows signifying individual virion particles. Images representative of two

preparations and 40 individual images observed for WT and ΔPRRA mutant. Scale bar represents 0.2 μm.

ACCELERATED ARTICLE PREVIEW

Reporting Summary

Nature Research wishes to improve the reproducibility of the work that we publish. This form provides structure for consistency and transparency in reporting. For further information on Nature Research policies, see our [Editorial Policies](#) and the [Editorial Policy Checklist](#).

Statistics

For all statistical analyses, confirm that the following items are present in the figure legend, table legend, main text, or Methods section.

n/a Confirmed

- The exact sample size (n) for each experimental group/condition, given as a discrete number and unit of measurement
- A statement on whether measurements were taken from distinct samples or whether the same sample was measured repeatedly
- The statistical test(s) used AND whether they are one- or two-sided
Only common tests should be described solely by name; describe more complex techniques in the Methods section.
- A description of all covariates tested
- A description of any assumptions or corrections, such as tests of normality and adjustment for multiple comparisons
- A full description of the statistical parameters including central tendency (e.g. means) or other basic estimates (e.g. regression coefficient) AND variation (e.g. standard deviation) or associated estimates of uncertainty (e.g. confidence intervals)
- For null hypothesis testing, the test statistic (e.g. F , t , r) with confidence intervals, effect sizes, degrees of freedom and P value noted
Give P values as exact values whenever suitable.
- For Bayesian analysis, information on the choice of priors and Markov chain Monte Carlo settings
- For hierarchical and complex designs, identification of the appropriate level for tests and full reporting of outcomes
- Estimates of effect sizes (e.g. Cohen's d , Pearson's r), indicating how they were calculated

Our web collection on [statistics for biologists](#) contains articles on many of the points above.

Software and code

Policy information about [availability of computer code](#)

Data collection FlexiWare v 8.1.3, Samtools v 1.9., Fastp v0.12, Nanozoomer, SWISS-Model, MacPyMol v 1.3.

Data analysis Data analysis conducted using PRISM 7.0 or Microsoft Excel.

For manuscripts utilizing custom algorithms or software that are central to the research but not yet described in published literature, software must be made available to editors and reviewers. We strongly encourage code deposition in a community repository (e.g. GitHub). See the Nature Research [guidelines for submitting code & software](#) for further information.

Data

Policy information about [availability of data](#)

All manuscripts must include a [data availability statement](#). This statement should provide the following information, where applicable:

- Accession codes, unique identifiers, or web links for publicly available datasets
- A list of figures that have associated raw data
- A description of any restrictions on data availability

The raw data that support the findings of this study are available from the corresponding author upon reasonable request. Spike modeling based on PDB 6ACD.

Field-specific reporting

Please select the one below that is the best fit for your research. If you are not sure, read the appropriate sections before making your selection.

Life sciences Behavioural & social sciences Ecological, evolutionary & environmental sciences

For a reference copy of the document with all sections, see [nature.com/documents/nr-reporting-summary-flat.pdf](https://www.nature.com/documents/nr-reporting-summary-flat.pdf)

Life sciences study design

All studies must disclose on these points even when the disclosure is negative.

Sample size	Sample sizes for experiments were determined by prior studies with coronaviruses that had power to detect changes in titer with a significance level of 0.05 (two-tailed). Gralinski, L.E., et al. mBio 4(2013).
Data exclusions	No data was excluded from the cacluation
Replication	In vitro experiments representative of at least 2 experiments with multiple samples per time point. In vivo experiment utilized multiple animal per group per time point and were from a single experiment (hamster) and 3 independent experiments (mice).
Randomization	Animals were assigned to groups at random. Cell for in vitro experiments were assigned at random.
Blinding	Investigators were not blinded during data collection or due to the limited capacity of workers able to complete high containment work. Data analysis was conducted by researcher who was not blinded.

Reporting for specific materials, systems and methods

We require information from authors about some types of materials, experimental systems and methods used in many studies. Here, indicate whether each material, system or method listed is relevant to your study. If you are not sure if a list item applies to your research, read the appropriate section before selecting a response.

Materials & experimental systems

n/a	Involved in the study
<input type="checkbox"/>	<input checked="" type="checkbox"/> Antibodies
<input type="checkbox"/>	<input checked="" type="checkbox"/> Eukaryotic cell lines
<input checked="" type="checkbox"/>	<input type="checkbox"/> Palaeontology and archaeology
<input type="checkbox"/>	<input checked="" type="checkbox"/> Animals and other organisms
<input checked="" type="checkbox"/>	<input type="checkbox"/> Human research participants
<input checked="" type="checkbox"/>	<input type="checkbox"/> Clinical data
<input checked="" type="checkbox"/>	<input type="checkbox"/> Dual use research of concern

Methods

n/a	Involved in the study
<input checked="" type="checkbox"/>	<input type="checkbox"/> ChIP-seq
<input checked="" type="checkbox"/>	<input type="checkbox"/> Flow cytometry
<input checked="" type="checkbox"/>	<input type="checkbox"/> MRI-based neuroimaging

Antibodies

Antibodies used	RabbitSARS-CoV Spike (S) specific antibodies (Novus Biologicals #NB100-56578) Horseradish peroxidase (HRP)-conjugated anti-rabbit antibody (Cell Signaling Technology #7074S) SARS-CoV Nucleocapsid (N) specific antibodies were generated in house by Dr. Shinji Makino provided as gift.
Validation	<p>Spike antibody- Orthogonal Validation- The target protein is examined with an antibody independent strategy and compared with results from an antibody-dependent strategy. A correlation between these two strategies indicates specificity between the antibody and its target protein. Examples of antibody independent techniques may include in situ hybridization, quantitative PCR, RNA-seq or mass spectrometry. Full length Spike protein transfected into UM92 cells was used as a positive control and an approximate 139 kDa band was observed. Dot Blot results using recombinant proteins for cross-reactivity testing revealed high reactivity to SARS-CoV-2 Spike Protein, 1000-1200 a.a. (NBP2-90973) and low/no reactivity towards MERS Spike 2 or H1N1 (NBP1-99041).</p> <p>HPR anti-rabit- This product is thoroughly validated with CST primary antibodies and will work optimally with the CST western immunoblotting protocol, ensuring accurate and reproducible results.</p> <p>SARS-CoV Nucleocapsid (N) specific antibodies (provided as a kind gift from Dr. Shinji Makino) - Previously published Harcourt et al. Emerg Infect Dis. 2020 Jun;26(6):1266-1273. doi: 10.3201/eid2606.200516. Epub 2020 Jun 17. The plasmid, pBM302, (Das D. and Suresh MR, J Virol Methods. 2006 Nov;137(2):343-6), was used to express SARS-CoV N protein, with a C-terminal His6 tag, to high levels within the inclusion bodies of E.coli and the recombinant protein was purified from the inclusion bodies by nickel-affinity column chromatography under denaturing conditions. The recombinant SARS-CoV N protein was refolded by stepwise dialysis against Tris/phosphate buffer with decreasing concentrations of urea to renature the protein. The renatured, full-length, SARS-CoV N protein was used to immunize rabbits to generate an affinity-purified rabbit anti-SARS-CoV N polyclonal antibody.</p>

Eukaryotic cell lines

Policy information about [cell lines](#)

Cell line source(s)	VeroE6 (gift from Ralph S. Baric, lab derivative of VERO C1008 ATCC CRL-1586); Calu3 2B4 (gift from Ralph Baric, lab derivative of ATCC HTB-55).
Authentication	None of the cells were authenticated
Mycoplasma contamination	VeroE6 and Calu3 2B4 cells are tested for mycoplasma contamination by RT-PCR periodically. Calu3 cells tested positive for mycoplasma contamination in July. Calu3 and Vero rederived from frozen stocks tested negative in August.
Commonly misidentified lines (See ICLAC register)	None

Animals and other organisms

Policy information about [studies involving animals](#); [ARRIVE guidelines](#) recommended for reporting animal research

Laboratory animals	Male Syrian hamsters (7-8 weeks old, 86–127g). Male and female K18-hACE C57BL/6J mice (strain: 2B6.Cg-Tg(K18-ACE2)2PrImn/J, 5-9 wks old) were obtained from The Jackson Laboratory. The ABSL-3 room was kept between 68-74 degrees Fahrenheit with 30-60% and 12h-12h light cycles (6AM-6PM)
Wild animals	Study did not involve wild animals
Field-collected samples	Study did not involve field collected samples
Ethics oversight	All procedures were conducted under an animal protocol approved by the UTMB Institutional Animal Care and Use Committee and complied with USDA guidelines in an AAALAC-accredited lab. Animal Care and Use Committee at the Washington University School of Medicine (assurance number A3381-01)

Note that full information on the approval of the study protocol must also be provided in the manuscript.